

## Synchronization of two spin-transfer-driven nano-oscillators coupled via magnetostatic fields

D. Mancilla-Almonacid,<sup>1</sup> Alejandro O. Leon,<sup>2</sup> R. E. Arias,<sup>3</sup> S. Allende,<sup>1</sup> and D. Altbir<sup>1</sup>

<sup>1</sup>*Departamento de Física, CEDENNA, Universidad de Santiago de Chile, USACH, Av. Ecuador 3493, Santiago, Chile*

<sup>2</sup>*Instituto de Física, Pontificia Universidad Católica de Valparaíso, Casilla 4059, Chile*

<sup>3</sup>*Departamento de Física, CEDENNA, Facultad de Ciencias Físicas y Matemáticas, Universidad de Chile, Av. Blanco Encalada 2008, Santiago, Chile*



(Received 7 December 2018; revised manuscript received 29 January 2019; published 11 March 2019)

The magnetization dynamics of nano-oscillators may be excited by both magnetic fields and spin-polarized currents. While the dynamics of single oscillators has been well characterized, the synchronization of several ones is not fully understood yet. An analytical and numerical study of the nonlinear dynamics of two magnetostatically coupled spin valves driven by spin-transfer torques is presented under the macrospin approximation. The oscillators interact via magnetostatic fields and exhibit a robust synchronized magnetization motion. We describe the magnetization dynamics of the system using the Landau-Lifshitz-Gilbert-Slonczewski equation. Using a modal decomposition technique, we describe the dynamics, synchronization, and competition of oscillatory modes as a function of the current density, and the geometrical parameters of the setup. Simulations of the Landau-Lifshitz-Gilbert-Slonczewski equation show good agreement with an approximate analytic solution.

DOI: [10.1103/PhysRevE.99.032210](https://doi.org/10.1103/PhysRevE.99.032210)

### I. INTRODUCTION

Spin-polarized electric currents can exert a torque in magnetic materials. This is known as the *spin-transfer torque* [1–4], and it can induce magnetic switching [4–6], stationary magnetic textures [7–9], and self-sustained oscillations [4,5,10,11]. The aforementioned oscillations are particularly interesting because they can be used to generate alternating signals from a purely dc electric current. The dynamics of single spin-transfer-driven devices has been largely studied from the experimental, analytic, and numeric points of view [3,4,10,12–14], while the collective behavior of several coupled oscillators is less explored. During the past years, the networks of spin-transfer-torque nano-oscillators (STNOs) have received a great deal of attention because they are candidates for the implementation of associative memories [15–17], where the degree of synchronization may be used as a measure of pattern recognition [17–19]. This synchronization may be obtained through several means, for example, by electrical connections or by spin-wave emission, and also by magnetostatic interactions [20–23]. The *synchronization* occurs when nonidentical oscillators tune their frequency due to their weak interaction [24]. In the case of oscillators with the same frequency, the synchronization manifests as a locking of the oscillation phases [24]. The synchronization phenomenon is beyond the field of nanomagnetism and is present in several branches of science including biological, mechanical, and electronic systems, among others [24].

Some examples of interacting oscillators include vortices coupled by dipolar fields [20,25] and spin valves interacting via spin pumping [26], electric currents [27], and spin-Hall [28] effect. Specifically, some works have investigated the synchronization of spin-torque nano-oscillators coupled through the magnetostatic interaction. For example, Locatelli

*et al.* [20] showed that the magnetostatic interaction between a pair of vortex-based spin-transfer nano-oscillators is an efficient mechanism to synchronize neighboring oscillators. In addition, Chen *et al.* [22] determined the critical current needed for synchronizing two nano-oscillators when the same or different currents are applied in both oscillators. Additionally, Zhang *et al.* [29] found that a two nano-oscillator system exhibits a locked-phase dynamic for small applied currents, and an unlocked one for large currents. Despite the advances made by these authors, it is important to note that, in an array of oscillators, the relative position between them plays an essential role because it may favor a parallel or antiparallel magnetization alignment. In a previous work [30], developing a linear study, we concluded that it is possible to control the normal modes of STNOs as well as the critical current densities necessary to induce oscillations of the magnetization by changing the relative position of the oscillators. Then, in order to understand the role that the position of the oscillators could play in the synchronization phenomenon, it is necessary to study the nonlinear dynamics of the magnetization.

In this article, we study the nonlinear dynamics of the uniform magnetization of two spin-transfer-driven thin disks that interact via magnetostatic fields, for two different relative positions between them. At the current-induced instability, the magnetizations of both disks oscillate with the same frequency. Furthermore, the difference between the oscillation phases remains constant. This synchronized motion can have two modes, namely the *in-phase* and the *antiphase* ones [30], where the phase difference is zero and  $\pi$ , respectively. To elucidate the behavior of the modes for larger currents, we derive simplified equations for the envelope of the in-phase (IP) and antiphase (AP) modes from the Landau-Lifshitz-Gilbert-Slonczewski (LLGS) equation. Using the analytical and numerical solutions of the simplified model, we

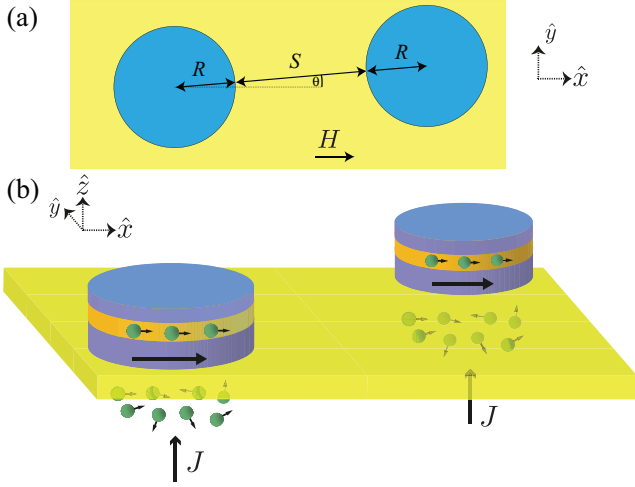


FIG. 1. (a) Top view and (b) side view of two nano-oscillators that are both driven by a spin-polarized current density  $J$  and coupled via magnetostatic fields. The magnetization  $\mathbf{M}_k = M_s \mathbf{m}_k$  of each free layer (upper disk in each valve) evolves according to the Landau-Lifshitz-Gilbert-Slonczewski equation.

characterize the competition of the modes and find the stable equilibria. In particular, we find a transition between the IP and the AP modes. For a finite range of electric current values, this transition goes through a *mixed-mode* with a finite contribution from both the IP and AP oscillations.

This paper is organized as follows: in Sec. II we describe the system under study, in Sec. III we present and discuss our results using analytical and numerical approaches, and finally in Sec. IV we present our conclusions and remarks.

## II. MODEL

Let us introduce a device known as a *spin valve*, in our case of cylindrical geometry. It consists of a disk made of a soft ferromagnetic material, whose magnetization is *free* to evolve in time, and that is grown on top of a bilayer composed by a fixed-magnetization material and a nonmagnetic spacer. When an electric current runs through the structure, the fixed layer polarizes the spin of the conduction electrons, then the current keeps its polarization as it passes through the nonmagnetic spacer, and later transfers angular momentum to the free layer, i.e., a spin transfer torque acting on the free layer is generated.

Then, we consider two identical cylindrical spin valves that are side by side, as illustrated in Fig. 1(a). The free layers are separated by a center-to-center distance of  $D = 2R + S$ , where  $S$  is the shortest distance between the surfaces of the free layers [see Fig. 1(b)]. The parameter  $\theta$  is the angle between the  $x$  axis and the line that connects the centers of both valves. The free layers have magnetizations  $\mathbf{M}_k = M_s \mathbf{m}_k$ , where  $k = \{1, 2\}$  is the valve label,  $M_s$  is the saturation magnetization that we assume equal for both materials, and  $\mathbf{m}_k = m_k^x \hat{\mathbf{x}} + m_k^y \hat{\mathbf{y}} + m_k^z \hat{\mathbf{z}}$ . The same magnetic field  $\mathbf{H} = 4\pi M_s h_x \hat{\mathbf{x}}$  (Gaussian system of units) and current density  $\mathbf{J} = J \hat{\mathbf{z}}$  are applied to each valve, as shown in Fig. 1. The magnetization dynamics of this system is governed by the

Landau-Lifshitz-Gilbert-Slonczewski equation [31]

$$\frac{d\mathbf{m}_k}{dt} = -\mathbf{m}_k \times \mathbf{h}_{\text{eff},k} + \alpha \mathbf{m}_k \times \frac{d\mathbf{m}_k}{dt} + \beta_J \mathbf{m}_k \times (\mathbf{m}_k \times \hat{\mathbf{x}}). \quad (1)$$

This equation is written within the macrospin approximation (that is, we consider that the magnetizations of the free layers are uniform), and with a dimensionless time  $t = 4\pi M_s \gamma t'$ , with  $\gamma = 1.76 \times 10^7$  (Oe s) $^{-1}$  the modulus of the gyromagnetic ratio and  $t'$  the original time in seconds. The vector  $\mathbf{h}_{\text{eff},k}$  is the effective field normalized by  $4\pi M_s$ . The dimensionless parameter  $\alpha$  is associated with the strength of the energy dissipation. The transfer of angular momentum by the current density  $J$  is proportional to the parameter  $\beta_J \equiv 2\pi \hbar \epsilon J / [(4\pi M_s)^2 e L]$ , where  $\epsilon$  is the polarization of the interface,  $0 \leq \epsilon \leq 1$ ,  $e$  is the modulus of the electron charge ( $\beta_J$  is positive when the current density flows from the fixed to the free layer), and  $L$  is the thickness of each free layer. The normalized effective field is

$$\mathbf{h}_{\text{eff},k} = h_x \hat{\mathbf{x}} - h_d m_k^z \hat{\mathbf{z}} + \mathbf{h}_{I,k}, \quad (2)$$

where the second term of the effective field corresponds to the self-magnetostatic interaction, and it leads to a hard  $z$  axis, or unfavorable direction for the magnetization. The coefficient  $h_d$  is the demagnetization factor which depends on the parameters  $R$  and  $L$  [see Appendix A, Eq. (A1)]. The last term accounts for the magnetostatic interaction between the nanopillars, and it represents a field that is exerted by pillar  $k'$  into pillar  $k$  [30]:

$$\begin{aligned} \mathbf{h}_{I,k} &= (g_x m_{k'}^x + g_{xy} m_{k'}^y) \hat{\mathbf{x}} + (g_y m_{k'}^y + g_{xy} m_{k'}^x) \hat{\mathbf{y}} + g_z m_{k'}^z \hat{\mathbf{z}}, \\ g_x(\theta) &= K_1 + K_2 \cos(2\theta), \\ g_y(\theta) &= K_1 - K_2 \cos(2\theta), \\ g_{xy}(\theta) &= K_2 \sin(2\theta), \\ g_z &= K_3, \end{aligned} \quad (3)$$

where  $K_j$  are functions of the geometrical parameters of the system  $R$ ,  $L$ , and  $D$ . Explicit formulas for  $K_j$  are shown in Eq. (A2), Appendix A.

In the case of single-valve devices, the self-sustained magnetization oscillations emerge when the applied current density injects enough energy to counterbalance the dissipation. For two nano-oscillators coupled via magnetostatic fields, there are two critical current densities which correspond to the ones of the in-phase and antiphase modes of oscillation [30]. If the applied current density exceeds the minimum critical current density of the system, the magnetizations of the free layers oscillate. To understand the behavior for larger current densities, a nonlinear study of the magnetization dynamics is necessary. We develop this analysis in the next section.

## III. RESULTS AND DISCUSSION

We focus on a system of two free layers composed of permalloy with  $M_s = 860$  emu/cm $^3$ . In relation to the geometrical parameters, we consider  $R = 50$  nm and  $L = 5$  nm. For these parameters  $h_d \approx 0.816$ ; and  $K_1 \approx 0.0025$ ,  $K_2 \approx 0.0054$ , and  $K_3 \approx -0.0050$ . To describe the magnetization dynamics by solving the LLGS equation, we consider

$h_x = 0.1$  ( $|\mathbf{H}| = 1$  kOe),  $\alpha = 0.01$ , and  $\epsilon = 0.11$ . We focus our attention on the magnetization dynamics around the equilibrium state defined as  $m_1^x = m_2^x = 1$ .

In the rest of this section we present and discuss results from analytic and numerical approaches.

### A. Analytical approach

When the current density attains its critical value  $\beta_J = \beta_{J,c}$ , the linear modes of the system correspond to an in-phase oscillation  $\delta \mathbf{m}_{ip} = A_0 \mathbf{v}_{ip} e^{i\omega_{ip}t} + \text{c.c.}$ , or an antiphase one  $\delta \mathbf{m}_{ap} = B_0 \mathbf{v}_{ap} e^{i\omega_{ap}t} + \text{c.c.}$ , where  $(\omega_{ip}, \mathbf{v}_{ip})$  and  $(\omega_{ap}, \mathbf{v}_{ap})$  are the frequencies and eigenvectors of the in-phase and antiphase modes [30], respectively. Explicit expressions for the vectors and frequencies are given in Appendix B. The complex amplitudes  $A_0$  and  $B_0$  are fixed by the initial conditions and c.c. stands for the complex conjugate. Above the instability point, i.e.,  $\beta_J > \beta_{J,c}$ , we propose the following change of variables:

$$\delta \mathbf{m} = A(t) \mathbf{v}_{ip} e^{i\omega_{ip}t} + B(t) \mathbf{v}_{ap} e^{i\omega_{ap}t} + \text{c.c.}, \quad (4)$$

in which the oscillation amplitudes become dynamical variables, and  $\delta \mathbf{m} = (m_1^y, m_1^z, m_2^y, m_2^z)^T$ , where the superindex  $T$  refers to the transpose of the quantity inside the brackets. The frequencies  $\omega_{ip/ap}$  and vectors  $\mathbf{v}_{ip/ap}$  are those obtained for  $\beta_J = \beta_{J,c}$ . The amplitudes of oscillation  $A(t)$  and  $B(t)$  depend on time and are complex quantities. We insert the ansatz of Eq. (4) in Eq. (1). Furthermore, we consider that the functions  $A(t)$ ,  $B(t)$ , and  $e^{2i(\omega_{ap}-\omega_{ip})t}$  are slow variables as compared to the self-sustained oscillations ( $|\dot{A}| \ll |\omega_{ip}A|$ ,  $|\dot{B}| \ll |\omega_{ap}B|$ , and  $|\omega_{ip} - \omega_{ap}| \ll \omega_{ip} \sim \omega_{ap}$ ). After a temporal average in the fast time scales, we could eliminate the terms containing fast oscillations. Then, we obtain the following expressions for the amplitudes:

$$\dot{A} = (\epsilon_1 - \eta_1 |A|^2 - \mu_1 |B|^2)A - \nu_1 e^{2i(\omega_{ap}-\omega_{ip})t} B^2 A^*, \quad (5a)$$

$$\dot{B} = (\epsilon_2 - \eta_2 |B|^2 - \mu_2 |A|^2)B - \nu_2 e^{2i(\omega_{ip}-\omega_{ap})t} A^2 B^*, \quad (5b)$$

where  $A^*$  and  $B^*$  stand for the complex conjugate of  $A$  and  $B$ , respectively. The coefficients of Eqs. (5a) and (5b) can be decomposed into their real and imaginary parts  $\epsilon_j = \epsilon_{jR} + i\epsilon_{jI}$ ,  $\eta_j = \eta_{jR} + i\eta_{jI}$ ,  $\mu_j = \mu_{jR} + i\mu_{jI}$ , and  $\nu_j = \nu_{jR} + i\nu_{jI}$ , where  $j = 1$  or  $2$ . The parameters  $\epsilon_{1R}$  and  $\epsilon_{2R}$  are interpreted as the energy injection that makes the amplitudes grow (if they are positive) or decay (if they are negative). These coefficients account for the competition between the spin-transfer and the Gilbert torques. The coefficients  $\eta_{1R}$  and  $\eta_{2R}$  represent the nonlinear dissipation mechanisms that saturate the amplitudes. The coefficients  $\{\mu_1, \mu_2\}$  and  $\{\nu_1, \nu_2\}$  account for the interaction between the two eigenmodes without and with frequency mixing ( $\omega_{ip} \sim \omega_{ap}$ ), respectively. The imaginary parts of the above parameters rule the phase dynamics. Note that  $\{\epsilon_j, \eta_j, \mu_j, \nu_j\}$  depend on the geometrical parameters of the system, such as the angle  $\theta$  and the distance  $S$ . Tables with a direct mapping from the coefficients of the LLGS equation to the ones of Eqs. (5a) and (5b) are shown in Appendix C.

The magnetization  $\delta \mathbf{m}$  has two superimposed oscillations at frequencies  $\omega_{ip}$  and  $\omega_{ap}$ , and their harmonics. We obtained equations for the envelope of those oscillations, Eqs. (5a) and (5b), by means of the rotating-wave-like change of variables

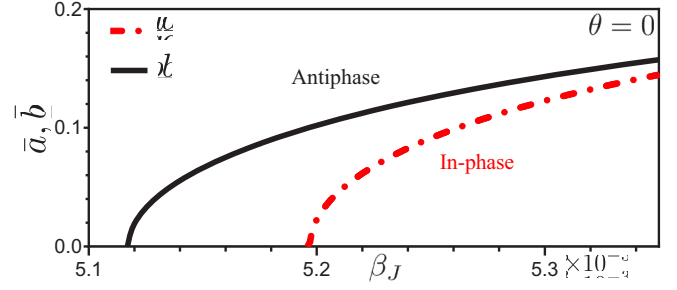


FIG. 2. Amplitude of single-mode oscillations as a function of the applied current density, for  $\theta = 0$  and  $S = 10$  nm. The free layers are made of Permalloy with  $R = 50$  nm and  $L = 5$  nm. The solid and dash-dotted lines correspond to the oscillation amplitude of the antiphase and the in-phase modes, respectively. The square-root form of the oscillation amplitude and the finite frequency are the hallmarks of supercritical Andronov-Hopf instabilities.

in Eq. (4), and by applying the orthonormality condition of Fourier functions. The modes have slightly different frequencies, and then there are interaction terms that obey the orthogonality condition approximately. Those terms manifest as time-dependent modal interaction. Using Eqs. (5a) and (5b), we look for single-mode oscillations with constant amplitude, i.e., solutions for  $|A| = \bar{a}$  and  $|B| = \bar{b}$ , where  $\bar{a}$  and  $\bar{b}$  are constants, i.e.,  $d|A|/dt = d|B|/dt = 0$ . We obtain the following three solutions:

$$(\bar{a}, \bar{b})_{s0} = (0, 0), \quad (6a)$$

$$(\bar{a}, \bar{b})_{s1} = \left( \sqrt{\frac{\epsilon_{1R}}{\eta_{1R}}}, 0 \right), \quad (6b)$$

$$(\bar{a}, \bar{b})_{s2} = \left( 0, \sqrt{\frac{\epsilon_{2R}}{\eta_{2R}}} \right), \quad (6c)$$

where  $(\bar{a}, \bar{b})_{s0}$  represents a static solution, while  $(\bar{a}, \bar{b})_{s1}$  and  $(\bar{a}, \bar{b})_{s2}$  represent single modes of oscillation that emerge via a supercritical Andronov-Hopf bifurcation [32]. Figure 2 illustrates the amplitude of these oscillatory single modes as a function of the applied current density for  $\theta = 0$ , i.e., the solutions of Eqs. (6b) and (6c). As shown in this figure, the system has two normal modes, the antiphase and the in-phase ones. Note that the antiphase mode emerges at a lower current in comparison with the in-phase mode. Below the critical density current that indicates growth of the antiphase mode, the system is static, that is,  $\delta \mathbf{m} = 0$ .

In addition to the simple antiphase and in-phase modes shown in Fig. 2, we search for nontrivial solutions of Eqs. (5a) and (5b). In particular, we use the following change of variables that eliminates the explicit temporal dependence of the terms proportional to  $\nu_j$  in these equations, namely,  $A = a e^{-i(\Delta\omega t + \psi)/2}$  and  $B = b e^{i(\Delta\omega t + \psi)/2}$ , where  $\Delta\omega = \omega_{ip} - \omega_{ap}$ . One obtains the new set of equations

$$\dot{a} = (\epsilon_{1R} - \eta_{1R} a^2 - [\mu_{1R} + \nu_{1R} \cos(2\psi) - \nu_{1I} \sin(2\psi)] b^2) a, \quad (7a)$$

$$\dot{b} = (\epsilon_{2R} - \eta_{2R} b^2 - [\mu_{2R} + \nu_{2R} \cos(2\psi) + \nu_{2I} \sin(2\psi)] a^2) b, \quad (7b)$$

$$\begin{aligned} \dot{\psi} = & -\Delta\omega + (\epsilon_{2I} - \epsilon_{1I}) + (\mu_{1I} - \eta_{2I})b^2 - (\mu_{2I} - \eta_{1I})a^2 \\ & + \cos(2\psi)(b^2v_{1I} - a^2v_{2I}) + \sin(2\psi)(a^2v_{2R} + b^2v_{1R}). \end{aligned} \quad (7c)$$

Usually, oscillators coupled via weak interactions exhibit a synchronized phase dynamics, where the coupling does not significantly alter the oscillation amplitudes [24]. However, in the present case, even if the magnetostatic coupling is relatively small compared to the magnetic and anisotropy fields, the oscillation phases are not the only relevant variables. Indeed, the dynamics of the oscillation amplitudes are relevant because the nano-oscillators operate at the onset of oscillatory instabilities (both modes have similar critical currents and similar frequencies). We may obtain approximate solutions of the set of Eqs. (7a)–(7c) by the following approximation:

$$a = \bar{a} + a_1 \sin(2\omega_0 t) + a_2 \cos(2\omega_0 t), \quad (8a)$$

$$b = \bar{b} + b_1 \sin(2\omega_0 t) + b_2 \cos(2\omega_0 t), \quad (8b)$$

$$\dot{\psi} = \omega_0, \quad (8c)$$

which we name *mixed-mode* state. The above ansatz represents a global oscillation in which both the in-phase and the antiphase modes contribute, that is,  $a, b \neq 0$ . Furthermore, the mode amplitudes oscillate at  $2\omega_0$ , with  $\omega_0$  an unknown frequency. This temporal dependence arises from the time-dependent modal interaction in Eqs. (5a) and (5b), and it originates from the frequency detuning,  $\omega_{ip} \neq \omega_{ap}$ . After replacing the ansatz of formulas into Eqs. (7a)–(7c), and using that Fourier modes are linearly independent, one obtains the solutions for  $\{\bar{a}, a_1, a_2\}$ ,  $\{\bar{b}, b_1, b_2\}$ , and  $\omega_0$ . Appendix D contains plots of these solutions as a function of  $\beta_J$ , which are characterized by a continuous growth of  $\bar{a}$  ( $\bar{b}$ ) for  $\theta = 0$  ( $\theta = \pi/2$ ). This supercritical behavior, in addition to the emergence of a frequency, allows us to recognize the supercritical Andronov-Hopf bifurcation of the antiphase (in-phase) oscillation for  $\theta = 0$  ( $\theta = \pi/2$ ). The direct numerical simulation of the magnetization equations will confirm this identification in the next subsection.

The amplitude of the oscillation of the magnetization,  $|\delta\mathbf{m}_j|$ , is defined as

$$|\delta\mathbf{m}_j| = \frac{1}{T} \int_{t_0}^{t_0+T} dt \sqrt{m_1^y(t)^2 + m_2^z(t)^2}. \quad (9)$$

Figure 3(a) illustrates  $|\delta\mathbf{m}_j|$  with  $t_0 = 0$  and  $T = 10^5$ . We obtain  $|\delta\mathbf{m}_j|$  for different solutions and  $\theta = 0$  by replacing the amplitudes from Eqs. (6b), (6c) and (8a)–(8c) in Eq. (4). This figure shows that the first mode that emerges is the antiphase one, characterized by an oscillation phase difference of  $\pi$ . To better understand the results in this figure, we study the magnetization behavior of the system in this regime. Figures 3(b) show the magnetization trajectories  $m_1^y \approx -m_2^y$  for  $\beta_J = 0.00513$  (left), 0.00522 (center), and 0.00535 (right), respectively. Figures 3(c) illustrate the phase diagram of points  $(m_1^y, m_2^y)$  from Figs. 3(b), respectively. The corresponding phase diagram given by Fig. 3(c) is known as *Lissajous figures* [24]. We note that, for  $\theta = 0$ , we have  $\omega_{ap} < \omega_{ip}$ , that is, the antiphase mode has lower frequency and consequently requires less energy to be excited [30].

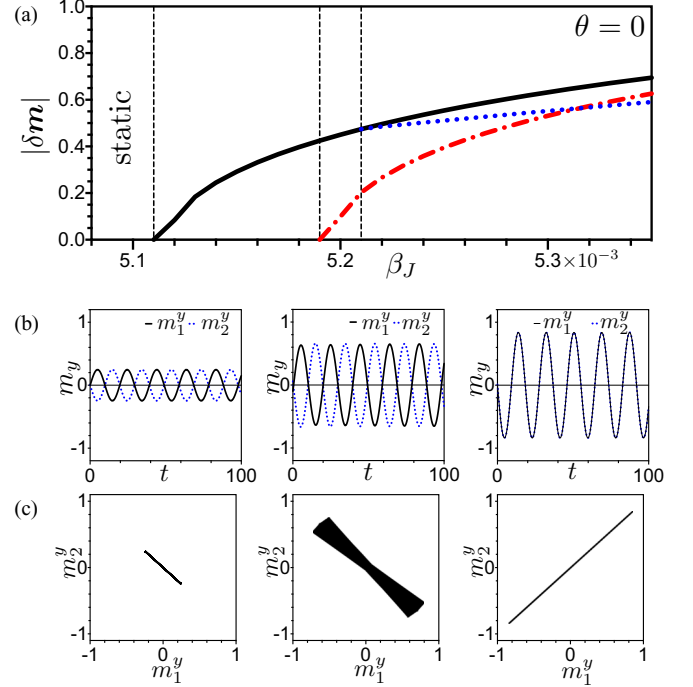


FIG. 3. (a) Oscillation amplitude of the magnetization,  $|\delta\mathbf{m}|$ , for  $\theta = 0$  and  $S = 10$  nm. The solid, dash-dotted, and dotted lines correspond to the amplitude of the oscillation of the antiphase, in-phase, and mixed modes, respectively. (b) Magnetization components  $m_1^y$  and  $m_2^y$  as functions of time for  $\theta = 0$  and  $S = 10$  nm, for different currents. At the left for the antiphase mode  $\beta_J = 0.00513$ , at the center for the mixed mode  $\beta_J = 0.00522$ , and at the right for the in-phase mode  $\beta_J = 0.00535$ . (c) Phase space in terms of the components  $m_1^y(t)$  and  $m_2^y(t)$ , and parametrized by the time  $t$ . The figures have the same current densities as in row (b), respectively.

Thus it is natural to observe this mode at the onset of the Andronov-Hopf instability [see the left panels of Figs. 3(b) and 3(c)]. Above a critical current, an oscillatory secondary instability of the system takes place. In this bifurcation, a small in-phase oscillation emerges around an antiphase orbit. In this case, the solution corresponds to a superposition of modes with a mixing of frequencies, namely *mixed-mode* state, where the in-phase and the antiphase modes coexist, and the dynamics is quasiperiodic. The corresponding phase diagram for this mixed state has a tielike shape as shown in Fig. 3(c) (center). When the energy injection increases, the system undergoes a third instability in which the antiphase contribution of the mixed-mode disappears, and the system stabilizes the in-phase oscillation [see the right panel of Figs. 3(b) and 3(c)]. Since the analytic study of the stability of periodic and quasiperiodic orbits is complicated in general, we specify the details of this bifurcation using the numerical results of the next subsection. Since the in-phase oscillation has a larger frequency and then requires more energy, it is expected that the stabilization of this state is only possible for larger electric currents. The mixed-mode solution is then the transition regime that mediates the existence of the IP and AP states. Appendix E shows the trajectories of the magnetization components  $m_1^y$  and  $m_2^y$  for a longer time, where we consider

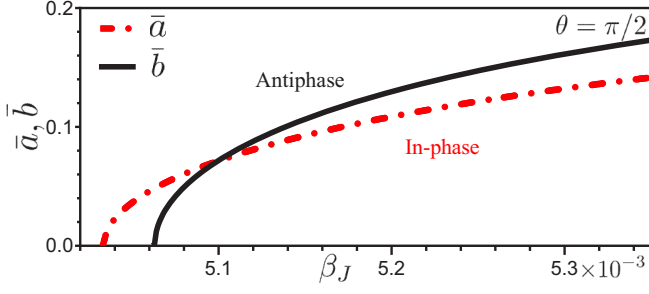


FIG. 4. Amplitude of single-mode oscillations as a function of the applied current density, for  $\theta = \pi/2$  and  $S = 10$  nm. The free layers are made of Permalloy with  $R = 50$  nm and  $L = 5$  nm. The solid and dash-dotted lines correspond to amplitude of oscillations for the antiphase and the in-phase modes, respectively.

Eqs. (8a), (8b), and (8c). As shown in this Appendix, the oscillation amplitudes are not constant.

Figures 4 and 5 illustrate analogous quantities for  $\theta = \pi/2$ . For the latter angle, the magnetostatic interaction inverts the energy consumption of each oscillation mode, i.e.,  $\omega_{ip} < \omega_{ap}$ . Thus the zones for  $\theta = \pi/2$  are inverted with respect to  $\theta = 0$ .

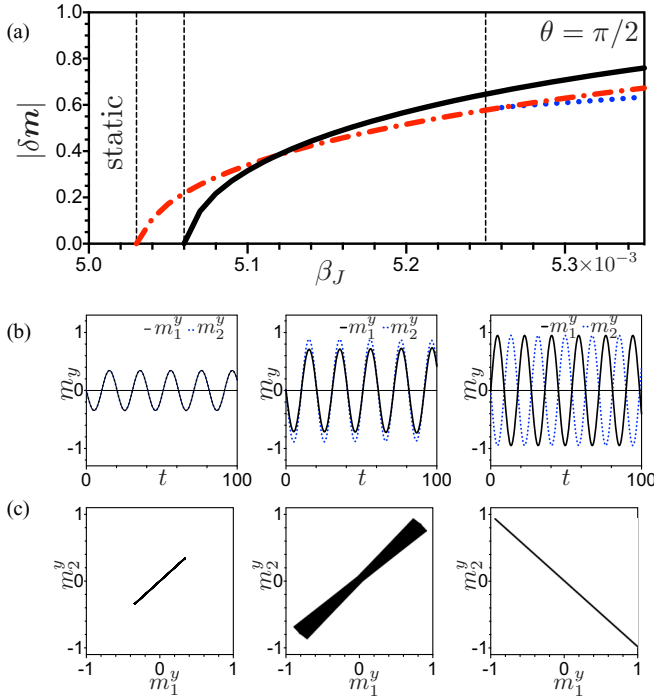


FIG. 5. (a) Amplitude of the oscillation of magnetization,  $|\delta \mathbf{m}|$ , for  $\theta = \pi/2$  and  $S = 10$  nm. The solid, dash-dotted, and dotted lines correspond to amplitude of oscillation of the magnetization of the antiphase, in-phase, and mixed modes, respectively. (b) Magnetizations  $m_1^y$  and  $m_2^y$  as a function of time for  $\theta = \pi/2$  and  $S = 10$  nm, for different currents. At the left for the in-phase mode  $\beta_J = 0.00507$ , at the center for the mixed mode  $\beta_J = 0.00527$ , and at the right for the antiphase mode  $\beta_J = 0.00530$ . (c) Phase space in terms of the components  $m_1^y(t)$  and  $m_2^y(t)$ , and parametrized by the time  $t$ . The figures have the same current densities as in row (b), respectively.

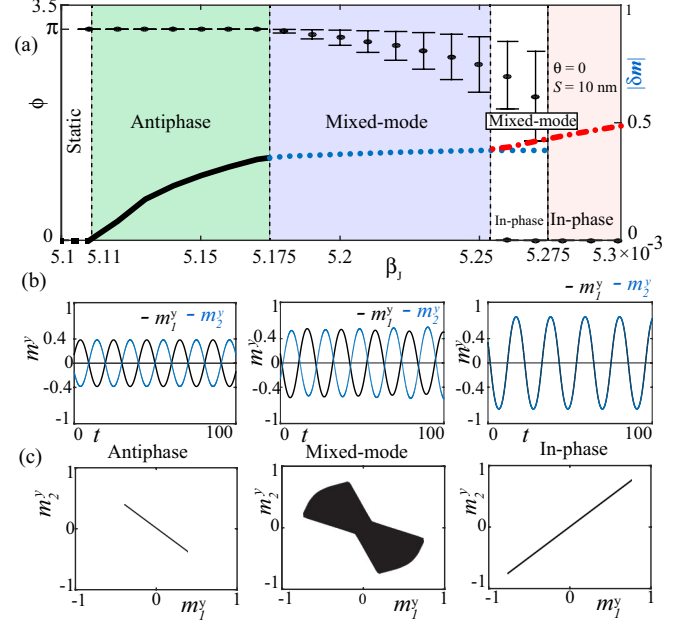


FIG. 6. Nonlinear dynamics of the magnetization for two magnetostatically coupled nano-oscillators for  $\theta = 0$ . (a) Amplitude of oscillation of magnetization and phase difference as a function of the current density. The left panel represents the antiphase mode (*antiphase zone*), the center panel the quasiperiodic state (*mixed-mode zone*), and the right panel the in-phase mode (*in-phase zone*). (b) Both magnetizations  $m_1^y$  and  $m_2^y$  as a function of time, for  $\beta_J = 0.00513$  (left),  $\beta_J = 0.00520$  (center), and  $\beta_J = 0.00535$  (right). (c) Phase space in terms of the components  $m_1^y(t)$  and  $m_2^y(t)$  for the same current densities used in (b).

To verify the predictions of the simplified model for the oscillation modes given by Eqs. (5a) and (5b), we conduct in the next subsection numerical simulations of the Landau-Lifshitz-Gilbert-Slonczewski equations (1).

## B. Numerical results

The numerical integration of the LLGS equation is conducted using a fifth-order Runge-Kutta method [33] with constant step size  $dt = 0.001$ , small enough to ensure the conservation of the magnetization norm for each free layer disk,  $\mathbf{m}_k^2 = 1$ . Figure 6 summarizes the trajectories of the magnetizations, for  $\theta = 0$  and  $S = 10$  nm, as a function of the parameter  $\beta_J$  proportional to the current density. We focus on the deviation from the stationary equilibrium,  $\delta \mathbf{m}_k = m_k^y(t) \hat{\mathbf{y}} + m_k^z(t) \hat{\mathbf{z}}$ . Figure 6(a) illustrates the phase difference,  $\phi$ , between the magnetizations, defined as

$$\phi = \arccos \left( \frac{\delta \mathbf{m}_1 \cdot \delta \mathbf{m}_2}{|\delta \mathbf{m}_1| |\delta \mathbf{m}_2|} \right), \quad (10)$$

and also the time-averaged oscillation envelope,  $|\delta \mathbf{m}_j|$ , from Eq. (9), where the times  $t_0 = 10^6$  and  $T = 10^5$  are much larger than the transient time and the oscillation period, respectively. We used those values for  $t_0$  and  $T$  throughout all the numerical part of the study. It is important to point out that we consider  $t_0 = 0$  for the analytical study because in that model the solution does not have a transient response, i.e., we obtain

the steady state for an arbitrary  $t$ . We define in Eq. (10) the relative angle  $\phi(t)$  between the magnetizations  $\delta\mathbf{m}_1$  and  $\delta\mathbf{m}_2$ , which is a measure of the degree of synchronization between the two nano-oscillators. In particular, when  $\phi(t)$  is constant in time, it means that the oscillators synchronize their phases. Figure 6 shows five zones: the first zone (*static*), for  $\beta_J < 0.00511$ , corresponds to the static equilibrium  $m_1^x = m_2^x = 1$ . At  $\beta_J = 0.00511$  occurs a supercritical Andronov-Hopf bifurcation resulting in a stable limit cycle; this is the beginning of the second zone (*antiphase*) which represents an antiphase oscillation, where  $m_1^y(t) \approx -m_2^y(t)$  with  $\phi \approx \pi$ . At  $\beta_J = 0.005175$ , a secondary instability of the system occurs; in this case it is a supercritical Andronov-Hopf bifurcation, in which the antiphase mode becomes unstable, resulting in a new stable limit cycle. This third zone (*mixed-mode*) represents a quasiperiodic state where the mixed mode bifurcated from an antiphase state. At the onset of this supercritical instability, the oscillatory trajectory is similar to the mode that became unstable. Finally, at  $\beta_J = 0.005255$  the in-phase oscillation is stabilized, and it coexists with the mixed mode until  $\beta_J = 0.005275$ , where the mixed mode is no longer observed.

The study of bifurcations of the periodic and quasiperiodic orbits is not a trivial task; however, from the previous subsection we know that the bifurcations at  $\beta_J = 0.005255$  and  $\beta_J = 0.005275$  are not related to the creation or destruction of the equilibria but to their stability (because these solutions exist in a wider region). Furthermore, the in-phase mode is always stable in the single-amplitude model (i.e.,  $\bar{b} \equiv 0$ ), and then the stability change at  $\beta_J = 0.005255$  must be from an unstable saddle-point-like to a stable one, where the unstable direction in the phase space flows towards the mixed-mode equilibrium. With a similar reasoning [32], we discard the saddle-node bifurcation at  $\beta_J = 0.005275$  (the mixed mode exists beyond that current value), and attribute its destabilization to the transition towards a saddle point or an unstable spiral. The last zone (*in-phase*) corresponds to an in-phase oscillation, where  $m_1^y(t) \approx m_2^y(t)$  with  $\phi \approx 0$ .

The in-phase and antiphase oscillations represent synchronized states, where the phase difference is locked. On the other hand, the mixed mode is characterized by a dynamic phase difference. The bar in Fig. 6(a) is the standard deviation of the temporal series of  $\phi(t)$ , and it plays the role of a dynamical indicator. Note that in the *mixed-mode* region the phase difference depends on time. This shows that the magnetization of each free layer is governed by two incommensurate frequencies,  $\omega_{ap}$  and  $\omega_{ip}$ . Thus the free layer magnetizations can accelerate and decelerate during the oscillation cycles. In addition, the maximum value of the phase difference increases with the current because the amplitude of the in-phase mode grows with the current, and it eventually becomes the dominant contribution to the mixed-mode solution. Figure 6(b) shows the magnetization components  $m_1^y$  and  $m_2^y$  as a function of time, for several current densities:  $\beta_J = 0.00513$  (left), that corresponds to the antiphase mode,  $\beta_J = 0.00520$  (center), that generates a mixed mode, and  $\beta_J = 0.00535$  (right), that corresponds to the in-phase mode. Figure 6(c) corresponds to the phase space of the system projected on the variables  $m_1^y(t)$  and  $m_2^y(t)$ , parametrized by the time  $t$ , for the respectively current densities of Fig. 6(b). As this figure illustrates, the

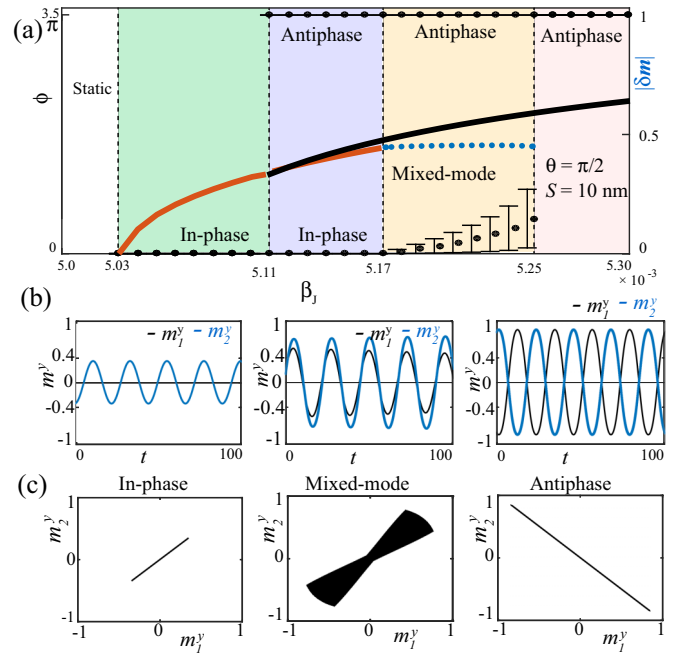


FIG. 7. Nonlinear dynamics of the magnetization for two magnetostatically coupled nano-oscillators for  $\theta = \pi/2$ . (a) Amplitude of oscillation of magnetization and phase difference as a function of the current density. The left panel represents the in-phase mode, the second panel represents bistability between the in-phase mode and antiphase modes, the third panel the quasiperiodic state (zone III), and the right panel the antiphase mode. (b) Both magnetizations  $m_1^y$  and  $m_2^y$  as a function of time, for  $\beta_J = 0.00507$  (left),  $\beta_J = 0.00520$  (center), and  $\beta_J = 0.00530$  (right). (c) Phase space in terms of the components  $m_1^y(t)$  and  $m_2^y(t)$  for the same current densities used in (b).

analytic solutions of Eqs. (6) and (8a)–(8c) are in good agreement with the simulations of the magnetic model with the static, antiphase, in-phase, and the mixed modes. Note that the numerical integration of the Landau-Lifshitz-Gilbert-Slonczewski equation reveals a *subcritical transition*, also known as a *first-order phase transition*, between the mixed mode and the in-phase mode. The subcriticality reflects as a bistability between the two aforementioned states in the lighter region of Fig. 6 between the mixed-mode and in-phase zones, in which the system selects one equilibrium or the other depending on the initial condition. We have not been able to find this bistability with the simple model presented in the previous subsection, partially because the analytic treatment of the stability of periodic orbits is, in general, a very hard task. Our analytic model allowed us to discover the solutions and their existing regions in the parameter space; however, finding the current intervals at which each state is stable is beyond the possibilities of our treatment.

On the other hand, Fig. 7 summarizes the trajectories of the magnetizations, for  $\theta = \pi/2$  and  $S = 10$  nm, as a function of the current density  $\beta_J$ . Figure 7(a) illustrates the amplitude of the oscillation of the magnetization,  $|\delta\mathbf{m}|$ , and the difference of phase  $\phi$ , as a function of the current density. We observe five different zones: the first zone (*static*), for  $\beta_J < 0.00503$ , represents the stable static equilibrium  $m_1^x = m_2^x = 1$ .

At  $\beta_J = 0.00503$  occurs a supercritical Andronov-Hopf [32] bifurcation resulting in a stable limit cycle. In this second zone (*in phase*), the stable limit cycle corresponds to an in-phase oscillation, where  $m_1^y \approx m_2^y$  with  $\phi \approx 0$ . At  $\beta_J = 0.00511$  the antiphase state is stabilized. In a similar reasoning to previous paragraphs, we conclude that the antiphase state is an unstable node for  $\beta_J < 0.00511$  and a stable one at  $\beta_J > 0.00511$ . In this third zone, there are two stable states (bistability) where one of them corresponds to an in-phase oscillation and the other to an antiphase oscillation. At  $\beta_J = 0.00517$  occurs a new supercritical Andronov-Hopf bifurcation, in which the in-phase mode becomes unstable. The new stable orbit corresponds to a quasiperiodic state bifurcated from the in-phase state. In this fourth zone, there are two stable dynamic states where one of them corresponds to a quasiperiodic state (*mixed mode*) and the other to an antiphase oscillation. Finally, at  $\beta_J = 0.00525$  the mixed mode destabilizes by becoming a saddle point or an unstable spiral, or by colliding with an unstable state that is not observable in the simulations. The last zone (*antiphase*) corresponds to an antiphase oscillation, where  $m_1^y \approx -m_2^y$  with  $\phi \approx \pi$ . Figure 7(b) shows the magnetizations  $m_1^y$  and  $m_2^y$  as a function of time, for different current densities.  $\beta_J = 0.00507$  (left) corresponds to the in-phase mode,  $\beta_J = 0.00520$  (center) gives a mixed mode, and  $\beta_J = 0.00530$  (right) corresponds to the antiphase mode. Figure 7(c) corresponds to the graph of the system of parametric equations,  $m_1^y(t)$  and  $m_2^y(t)$ , where  $t$  is the parameter, for the respective current densities in Fig. 7(b). As this figure illustrates, the analytic solutions of Eqs. (6) and Eqs. (8a)–(8c) are in good agreement with the simulations of the magnetic model for the static, antiphase, in-phase, and the mixed modes.

So far, we have analyzed two relevant angles, namely  $\theta = 0$  and  $\theta = \pi/2$ , each one of them showing different behavior. There are two intermediate angles,  $\theta_1 \approx 0.64$ , where the frequencies of the two modes (in-phase and antiphase) are identical, and  $\theta_2 \approx 1.08$ , where the critical current densities of the two modes are equal [30]. These two angles separate the two aforementioned cases ( $\theta = 0$  and  $\theta = \pi/2$ ), as it is shown in Fig. 8. This figure illustrates a simplified phase diagram in the current-angle parameter space. It is obtained slowly increasing in time the dc current at a fixed given angle: the initial current is below critical values, and different initial conditions are tested. When the current is below its critical value for all the modes the system is in the static phase, and as the current increases other phases appear (there are approximate limits in this diagram). Then, the first mode that we observe is the one with the lowest critical current. As the current increases, the mixed mode exists and, finally, we observe the mode with the biggest critical current. We observe that, for  $0 \leq \theta \leq \theta_1$  and  $\theta_2 \leq \theta \leq \pi/2$ , the results are qualitatively consistent with the ones shown in Figs. 6 and 7, respectively (notice that Fig. 8 corresponds to an increasing current direction). Now, if we consider a fixed angle  $\theta \lesssim 0.64$  we observe the antiphase mode for low currents and the in-phase one for large currents. The mixed mode exists in an intermediate region. For  $\theta \gtrsim 1.08$  occurs the opposite, i.e., the in-phase and antiphase modes are stable in the low and high current limits, respectively, and the mixed-mode state is also

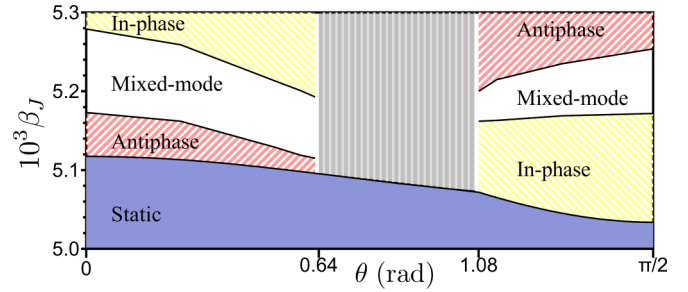


FIG. 8. Phase diagram in the current-angle parameter space, done under the assumption that the dc current is increased from a low value (i.e., below the critical current of any mode). Different initial conditions are tested. For  $\theta \lesssim 0.64$ , as the current increases, first an antiphase mode appears, then the mixed mode occurs, and finally the in-phase mode is observed. For  $\theta \gtrsim 1.08$ , as the current increases, the first mode that appears is the in-phase mode, then we observe a mixed mode, and finally the antiphase mode. In the intermediary zone,  $0.64 \lesssim \theta \lesssim 1.08$ , the behavior is not simple to analyze due to their similar frequencies and critical currents.

in the intermediate region. If we compare results depicted in Fig. 8 with results in Figs. 6(a) and 7(a), we only observe one of the branches of the magnetization dynamics, and we do not observe the bistability zones that appear in the previous figures. To observe the other branch, the current density should be decreased from a high value. For angles in the range  $0.64 \lesssim \theta \lesssim 1.08$  (gray zone in Fig. 8), the mode with the lowest critical current is the antiphase mode, with the biggest frequency. This behavior is opposite to what occurs for the other ranges of angles, where the mode with the lowest critical current also has the lowest frequency [30]. Additionally, for  $\theta \approx 0.64$ , the frequencies of both modes are very similar and the mixing between them is strong, while, for  $\theta \approx 1.08$ , the critical current densities of both modes are very similar, and the bistability zone between the in-phase and antiphase modes is very narrow. In this range of angles we principally observe two behaviors depending on the initial conditions: if the antiphase mode is excited first (for lower currents), for higher currents we do not observe the mixed mode, but if the in-phase mode is excited first (for lower currents), then we observe the mixed mode (for higher currents). The behavior for this range of angles should be studied in detail in another work.

To finalize, if we reduce the magnetostatic interaction between the oscillators by increasing the distance  $S$ , we observe that the zone of stability of the antiphase and the mixed states decreases for  $\theta \leq \theta_1$  [see Fig. 6(a) for  $S = 10$  nm and Fig. 9(a) for  $S = 50$  nm at  $\theta = 0$ ]. In these figures, we observe that the antiphase zone changes from  $0.00511 \leq \beta_J \leq 0.005175$  ( $\Delta\beta_J = 6.5 \times 10^{-5}$ ) to  $0.00508 \leq \beta_J \leq 0.00511$  ( $\Delta\beta_J = 3 \times 10^{-5}$ ) when we change  $S$  from 10 nm to 50 nm. The corresponding change for the mixed-mode zone goes from  $0.005175 \leq \beta_J \leq 0.00525$  ( $\Delta\beta_J = 7.5 \times 10^{-5}$ ) to  $0.00511 \leq \beta_J \leq 0.00513$  ( $\Delta\beta_J = 2 \times 10^{-5}$ ), respectively. Consistently, the zone where the in phase is stable becomes larger [see Figs. 6(a) and 9(a)]. A similar situation is obtained for  $\theta \geq \theta_2$ , where the in-phase and mixed-mode zones decrease when we increase the distance between the

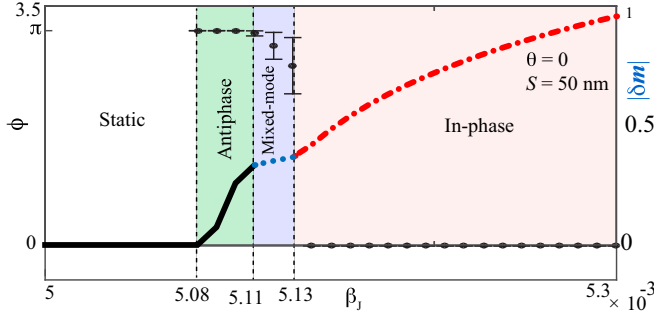


FIG. 9. Nonlinear dynamics of two magnetostatic coupled nano-oscillators for  $\theta = 0$  and  $S = 50$  nm. The free layers are made of Permalloy with  $R = 50$  nm and  $L = 5$  nm. The first zone shows the static equilibrium, for larger currents, there is an antiphase mode, and then a quasiperiodic state. The rightmost zone is the in-phase mode.

oscillators, while the zone where the antiphase is stable becomes larger. The stability zones become narrower and we could not find the bistability regions present for  $S = 10$  nm. Then, the phenomenon of synchronization depends on the magnetostatic interaction.

IV. CONCLUSIONS AND REMARKS

In summary, through nonlinear analytic and numerical simulations we have studied the magnetization dynamics of spin-transfer-driven oscillators coupled via magnetostatic fields, as a function of the current density, the relative position of the oscillators, and the distance between them. For most values of the density current, the system exhibits a synchronized motion of the magnetizations. In this regime, the difference between the oscillation phases of the free layers remains nearly zero for an in-phase mode and  $\pi$  for an antiphase mode. Those modes interact and compete and, depending on the particular values of the parameters and the initial conditions, the system chooses one of them. For example, for free layers arranged collinear to the magnetic field ( $\theta = 0$ ), the antiphase mode dominates for smaller density currents, and the in-phase one dominates for the larger density currents. The transition between the two regimes, as mentioned above, is characterized by a mixed-mode state, in which both the antiphase and in-phase modes participate with a finite amplitude of oscillation. Concerning the distance between the valves, if we increase the magnetostatic coupling by approaching them, the zone where the in-phase (antiphase) mode is stable becomes larger for  $\theta = 0$  ( $\theta = \pi/2$ ). When the free layers are well separated, the first zones of the stability diagram get narrower. However, the phase locking still exists, as is expected from a system exhibiting synchronization. Thus these results could be used

TABLE I. Values of the parameters  $K_1$ ,  $K_2$ , and  $K_3$  for  $S = 10$  nm,  $S = 50$  nm, and  $S = 100$  nm.

	$S = 10$ nm	$S = 50$ nm	$S = 100$ nm
$K_1$	0.002510	0.0006275	0.0002281
$K_2$	0.005441	0.001648	0.0006390
$K_3$	-0.005021	-0.001255	-0.0004562

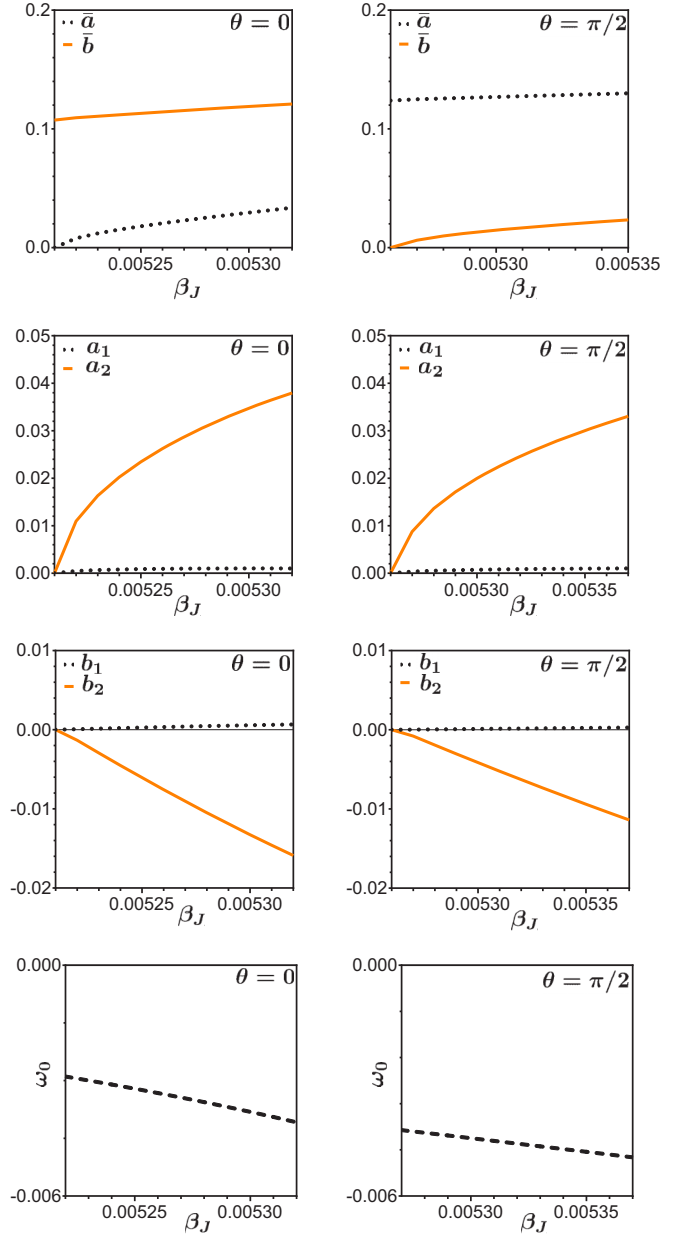


FIG. 10. Parameters of Eqs. (8a)–(8c) as a function of the applied current density.  $\bar{a}$ ,  $\bar{b}$ ,  $a_1$ ,  $a_2$ ,  $b_1$ ,  $b_2$ , and  $\omega_0$ , for  $S = 10$  nm and  $\theta = 0$  (left panel), and for  $\theta = \pi/2$  (right panel).

as one step in the quest for the design and control of spin-transfer-driven oscillators in associative memories.

ACKNOWLEDGMENTS

We acknowledge financial support in Chile from FONDECYT Grants No. 1161018, No. 1160198, and No. 1170781, and Financiamiento Basal para Centros Científicos y Tecnológicos de Excelencia FB 0807. This material is based upon work supported by the Air Force Office of Scientific Research under Grant No. FA9550-18-1-0438. D.M.-A. acknowledges Postdoctorado FONDECYT 2018, folio No. 3180416.

TABLE II. Values of the parameters of Eqs. (5a) and (5b) as a function of  $\beta_J$  for  $S = 10$  nm,  $S = 50$  nm, and  $S = 100$  nm at  $\theta = 0$  and  $\theta = \pi/2$ .

	$S = 10$ nm, $\theta = 0$	$S = 50$ nm, $\theta = 0$	$S = 100$ nm, $\theta = 0$
$\epsilon_1$	$\beta_J - 0.00520$	$\beta_J - 0.00511$	$\beta_J - 0.00509$
$\eta_1$	$(0.0428 + 1.02i) - 9.37\beta_J$	$(0.0430 + 0.885i) - 9.897\beta_J$	$(0.0430 + 0.845i) - 10.1\beta_J$
$\mu_1$	$(0.0846 + 1.55i) - 19.5\beta_J$	$(0.0858 + 1.61i) - 20.1\beta_J$	$(0.086 + 1.63i) - 20.2\beta_J$
$\nu_1$	$(0.0420 + 0.678i) - (9.66 + 0.00614i)\beta_J$	$(0.0428 + 0.776i) - (10.0 + 0.00258i)\beta_J$	$(0.0430 + 0.802i) - (10.1 + 0.00109i)\beta_J$
$\epsilon_2$	$\beta_J - 0.00512$	$\beta_J - 0.00509$	$\beta_J - 0.00508$
$\eta_2$	$(0.0427 + 0.914i) - 9.75\beta_J$	$(0.0430 + 0.845i) - 10.1\beta_J$	$(0.0431 + 0.829i) - 10.12\beta_J$
$\mu_2$	$(0.0836 + 1.52i) - 18.8\beta_J$	$(0.0853 + 1.60i) - 19.8\beta_J$	$(0.0858 + 1.62i) - 20.1\beta_J$
$\nu_2$	$(0.0407 + 0.761i) - (9.46 - 0.00601i)\beta_J$	$(0.0423 + 0.803i) - (9.93 - 0.00256i)\beta_J$	$(0.0428 + 0.813i) - (10.1 - 0.00109i)\beta_J$
	$S = 10$ nm, $\theta = \pi/2$	$S = 50$ nm, $\theta = \pi/2$	$S = 100$ nm, $\theta = \pi/2$
$\epsilon_1$	$\beta_J - 0.00506$	$\beta_J - 0.00507$	$\beta_J - 0.00508$
$\eta_1$	$(0.0420 + 0.899i) - 9.64\beta_J$	$(0.0428 + 0.840i) - 10.02\beta_J$	$(0.0430 + 0.827i) - 10.1\beta_J$
$\mu_1$	$(0.0915 + 1.76i) - 22.6\beta_J$	$(0.0876 + 1.68i) - 20.9\beta_J$	$(0.0867 + 1.65i) - 20.6\beta_J$
$\nu_1$	$(0.0465 + 0.774i) - (10.9 + 0.0294i)\beta_J$	$(0.0440 + 0.810i) - (10.4 + 0.00768i)\beta_J$	$(0.0434 + 0.816i) - (10.2 + 0.00286i)\beta_J$
$\epsilon_2$	$\beta_J - 0.00503$	$\beta_J - 0.00506$	$\beta_J - 0.00507$
$\eta_2$	$(0.0447 + 0.569i) - 11.3\beta_J$	$(0.0435 + 0.752i) - 10.47\beta_J$	$(0.0433 + 0.794i) - 10.3\beta_J$
$\mu_2$	$(0.08328 + 1.616i) - 19.28\beta_J$	$(0.0854 + 1.63i) - 20.0\beta_J$	$(0.0859 + 1.64i) - 20.2\beta_J$
$\nu_2$	$(0.0422 + 0.936i) - (10.0 - 0.0269i)\beta_J$	$(0.0428 + 0.856i) - (10.1 - 0.00750i)\beta_J$	$(0.0430 + 0.834i) - (10.1 - 0.00283i)\beta_J$

### APPENDIX A: MAGNETOSTATIC FIELDS

In this section we show the expressions for the magnetostatic fields related to the self-magnetostatic field and the magnetostatic interaction field between the nano-oscillators. The normalized self-magnetostatic field points along the  $z$  axis with  $\mathbf{h}_k^d = -h_d m_k^z \hat{\mathbf{z}}$ , where the demagnetization factor  $h_d$  depends on the geometrical parameters of the nano-oscillator, i.e., the thickness  $L$  and the radius  $R$ , with  $h_d$  given by [30]

$$h_d = 1 + \frac{3}{L/R} \int_0^\infty J_0'(q)^2 \frac{(1 - e^{-qL/R} - qL/R)}{q^2} dq, \quad (\text{A1})$$

where  $J_0'(q) = -J_1(q)$  is the derivative of  $J_0(q)$  and  $J_n$  is the Bessel function of the first kind and order  $n$ . The demagnetizing field is obtained from the functional derivative of the self-magnetostatic energy, and it is averaged over the disk volume. For  $L = 5$  nm and  $R = 50$  nm, we have  $h_d \approx 0.8155$ .

The normalized magnetostatic interaction field between the free layers is defined as a function of the  $K_1$ ,  $K_2$ , and  $K_3$  parameters [30] appearing in Eq. (3). These are

$$\begin{aligned} K_1 &= \frac{1}{L/D} \int_0^\infty J_1^2(qR/D) J_0(q) \frac{(1 - e^{-qL/D} - qL/D)}{q^2} dq, \\ K_2 &= -\frac{1}{L/D} \int_0^\infty J_1^2(qR/D) J_2(q) \frac{(1 - e^{-qL/D} - qL/D)}{q^2} dq, \\ K_3 &= \frac{2}{L/D} \int_0^\infty J_1^2(qR/D) J_0(q) \frac{(e^{-qL/D} - 1)}{q^2} dq, \end{aligned} \quad (\text{A2})$$

where  $D = 2R + S$ . Table I shows the values of these parameters as a function of  $S$ . We observe that, as  $S$  increases, these quantities approach zero.

### APPENDIX B: OSCILLATION FREQUENCIES AND MODES AT THE INSTABILITY POINT

The linear modes of the system of two coupled thin disks correspond to an in-phase oscillation  $\delta \mathbf{m}_{ip} = A_0 \mathbf{v}_{ip} e^{i\omega_{ip} t} + \text{c.c.}$

and an antiphase one  $\delta \mathbf{m}_{ap} = B_0 \mathbf{v}_{ap} e^{i\omega_{ap} t} + \text{c.c.}$ . We have that  $(\omega_{ip}, \mathbf{v}_{ip})$  and  $(\omega_{ap}, \mathbf{v}_{ap})$  are the frequencies and eigenvectors of the in-phase and antiphase modes, respectively.

The explicit expressions of the eigenfrequencies are [30]

$$\begin{aligned} \omega_{ip} &= \sqrt{h_x + g_x - g_y \sqrt{h_x + g_x + h_d - g_z}}, \\ \omega_{ap} &= \sqrt{h_x + g_x + g_y \sqrt{h_x + g_x + h_d + g_z}}. \end{aligned} \quad (\text{B1})$$

The explicit expressions of the eigenvectors are [30]

$$\mathbf{v}_{ip} = \begin{pmatrix} m_1 + m_3 + \omega_{ip} \\ -(m_2 + m_4) \\ m_1 + m_3 + \omega_{ip} \\ -(m_2 + m_4) \end{pmatrix}, \quad \mathbf{v}_{ap} = \begin{pmatrix} -(m_1 - m_3 + \omega_{ap}) \\ m_2 - m_4 \\ (m_1 - m_3 + \omega_{ap}) \\ -(m_2 - m_4) \end{pmatrix}, \quad (\text{B2})$$

where

$$\begin{aligned} m_1 + m_3 &= \omega_0 + (\lambda^2 + \mu^2)g_x - [(\lambda + \mu)^2 g_y + (\lambda - \mu)^2 g_z]/2, \\ m_2 + m_4 &= -2\lambda\mu g_x + [(\lambda + \mu)^2 g_y - (\lambda - \mu)^2 g_z]/2, \\ m_1 - m_3 &= \omega_0 + (\lambda^2 + \mu^2)g_x + [(\lambda + \mu)^2 g_y + (\lambda - \mu)^2 g_z]/2, \\ m_2 - m_4 &= -2\lambda\mu g_x - [(\lambda + \mu)^2 g_y - (\lambda - \mu)^2 g_z]/2, \end{aligned}$$

and

$$\begin{aligned} \omega_0 &= \sqrt{h_x(h_x + h_d)}, \\ \lambda &= \sqrt{\frac{h_x + h_d/2 + \omega_0}{2\omega_0}}, \\ \mu &= \sqrt{\frac{h_x + h_d/2 - \omega_0}{2\omega_0}}. \end{aligned}$$

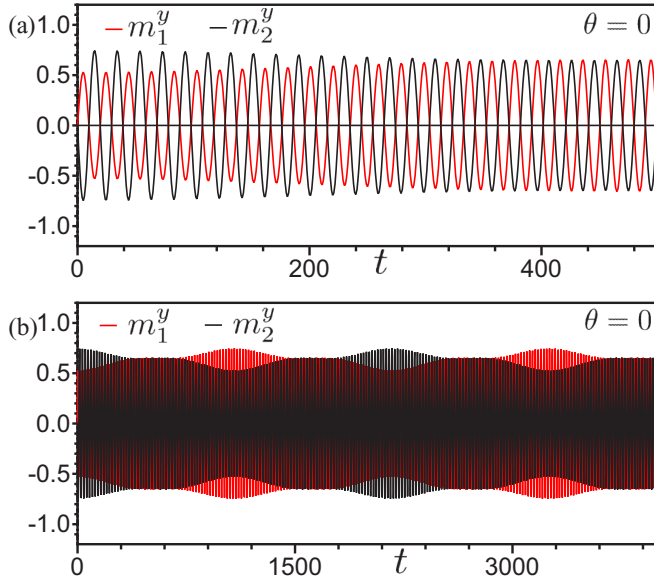


FIG. 11. Magnetization components  $m_1^y$  and  $m_2^y$  as a function of time for maximum time (a)  $t = 500$  and (b)  $t = 4000$ , and for  $\beta_J = 5.22 \times 10^{-3}$  and  $\theta = 0$ .

#### APPENDIX C: PARTICULAR PARAMETERS OF EQS. (5a) AND (5b)

Table II contains the values of the parameters  $\epsilon_1$ ,  $\eta_1$ ,  $\mu_1$ ,  $\nu_1$ ,  $\epsilon_2$ ,  $\eta_2$ ,  $\mu_2$ , and  $\nu_2$  as a function of  $\beta_J$  for  $\theta = 0$  and  $\theta = \pi/2$  at  $S = 10, 50$ , and  $100$  nm. These values are obtained by mapping Eq. (1) into Eqs. (5a) and (5b).

#### APPENDIX D: PARAMETERS OF EQS. (8a)–(8c)

In this section we show the parameters of Eqs. (8a)–(8c) as a function of the applied current density. Figure 10 illustrates

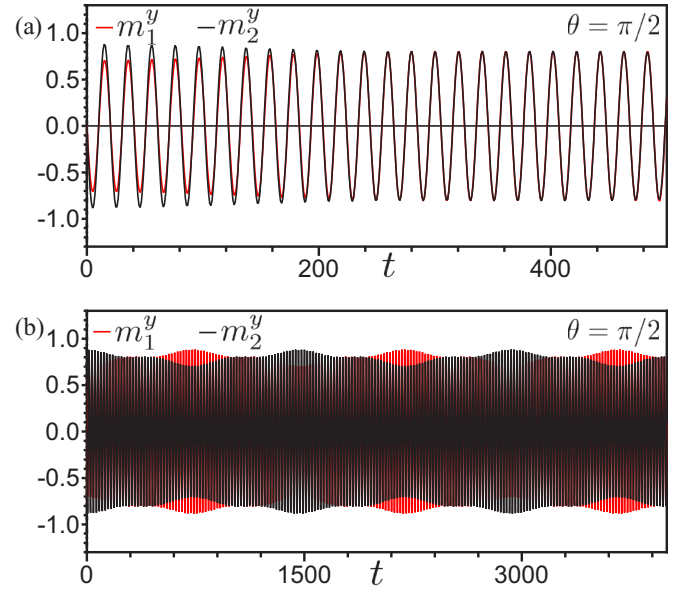


FIG. 12. Magnetization components  $m_1^y$  and  $m_2^y$  as a function of time for maximum time (a)  $t = 500$  and (b)  $t = 4000$ , and for  $\beta_J = 5.27 \times 10^{-3}$  and  $\theta = \pi/2$ .

$\bar{a}$ ,  $\bar{b}$ ,  $a_1$ ,  $a_2$ ,  $b_1$ ,  $b_2$ , and  $\omega_0$ , for  $S = 10$  nm and  $\theta = 0$  (left panel), and for  $\theta = \pi/2$  (right panel).

#### APPENDIX E: MAGNETIZATION COMPONENTS AS A FUNCTION OF TIME

In this section, we show the trajectory of the magnetization components  $m_1^y$  and  $m_2^y$  for a larger time interval, by using the solutions of Eqs. (8a), (8b), and (8c). For  $\theta = 0$ , we consider  $\beta_J = 5.22 \times 10^{-3}$  (Fig. 11) and for  $\theta = \pi/2$ , we use  $\beta_J = 5.27 \times 10^{-3}$  (Fig. 12). It can be observed that the oscillation amplitudes of the magnetizations are not constant.

- [1] J. C. Slonczewski, Current-driven excitation of magnetic multilayers, *J. Magn. Magn. Mater.* **159**, L1 (1996).
- [2] L. Berger, Emission of spin waves by a magnetic multilayer traversed by a current, *Phys. Rev. B* **54**, 9353 (1996).
- [3] D. C. Ralph and M. D. Stiles, Spin transfer torques, *J. Magn. Magn. Mater.* **320**, 1190 (2008).
- [4] *Concepts in Spin Electronics*, edited by S. Maekawa (Oxford University Press, Oxford, 2006).
- [5] K. J. Lee, A. Deac, O. Redon, J. P. Nozieres, and B. Dieny, Excitations of incoherent spin-waves due to spin-transfer torque, *Nat. Mater.* **3**, 877 (2004).
- [6] Z. Diao, Z. Li, S. Wang, Y. Ding, A. Panchula, E. Chen, L.-C. Wang, and Y. Huai, Spin-transfer torque switching in magnetic tunnel junctions and spin-transfer torque random access memory, *J. Phys.: Condens. Matter* **19**, 165209 (2007).
- [7] O. M. Volkov, V. P. Kravchuk, D. D. Sheka, F. G. Mertens, and Y. Gaididei, Periodic magnetic structures generated by spin-polarized currents in nanostripes, *Appl. Phys. Lett.* **103**, 222401 (2013).
- [8] A. O. Leon and M. G. Clerc, Spin-transfer-driven nano-oscillators are equivalent to parametric resonators, *Phys. Rev. B* **91**, 014411 (2015).
- [9] Z. D. Li, Q. Y. Li, L. Li, and W. Liu, Soliton solution for the spin current in a ferromagnetic nanowire, *Phys. Rev. E* **76**, 026605 (2007).
- [10] S. I. Kiselev, J. C. Sankey, I. N. Krivorotov, N. C. Emley, R. J. Schoelkopf, R. A. Buhrman, and D. C. Ralph, Microwave oscillations of a nanomagnet driven by a spin-polarized current, *Nature (London)* **425**, 380 (2003).
- [11] A. Slavin and V. Tiberkevich, Nonlinear auto-oscillator theory of microwave generation by spin-polarized current, *IEEE Trans. Magn.* **45**, 1875 (2009).
- [12] J. A. Katine, F. J. Albert, R. A. Buhrman, E. B. Myers, and D. C. Ralph, Current-Driven Magnetization Reversal and Spin-Wave Excitations in Co/Cu/Co Pillars, *Phys. Rev. Lett.* **84**, 3149 (2000).
- [13] J. Z. Sun, Spin-current interaction with a monodomain magnetic body: A model study, *Phys. Rev. B* **62**, 570 (2000).

- [14] D. Mancilla-Almonacid and R. E. Arias, Instabilities of spin torque driven auto-oscillations of a ferromagnetic disk magnetized in plane, *Phys. Rev. B* **93**, 224416 (2016).
- [15] F. C. Hoppensteadt and E. M. Izhikevich, Oscillatory Neurocomputers with Dynamic Connectivity, *Phys. Rev. Lett.* **82**, 2983 (1999).
- [16] D. E. Nikonov, G. Csaba, W. Porod, T. Shibata, D. Voils, D. Hammerstrom, I. A. Young, and G. I. Bourianoff, Coupled-oscillator associative memory array operation for pattern recognition, *IEEE J. Explor. Sol.-State Comput. Dev. Circuits* **1**, 85 (2015).
- [17] D. Vodenicarevic, N. Locatelli, F. Abreu Araujo, J. Grollier, and D. Querlioz, A nanotechnology-ready computing scheme based on a weakly coupled oscillator network, *Sci. Rep.* **7**, 44772 (2017).
- [18] P. Maffezzoni, B. Bahr, Z. Zhang, and L. Daniel, Oscillator array models for associative memory and pattern recognition, *IEEE Trans. Circuits Syst. I* **62**, 1591 (2015).
- [19] E. Vassilieva, G. Pinto, J. A. de Barros, and P. Suppes, Learning pattern recognition through quasi-synchronization of phase oscillators, *IEEE Trans. Neural Netw.* **22**, 84 (2011).
- [20] N. Locatelli, A. Hamadeh, F. Abreu Araujo, A. D. Belanovsky, P. N. Skirdkov, R. Lebrun, V. V. Naletov, K. A. Zvezdin, M. Muñoz, J. Grollier, O. Klein, V. Cros, and G. de Loubens, Efficient synchronization of dipolarly coupled vortex-based spin transfer nano-oscillators, *Sci. Rep.* **5**, 17039 (2015).
- [21] A. D. Belanovsky, N. Locatelli, P. N. Skirdkov, F. A. Araujo, K. A. Zvezdin, J. Grollier, V. Cros, and A. K. Zvezdin, Numerical and analytical investigation of the synchronization of dipolarly coupled vortex spin-torque nano-oscillators, *Appl. Phys. Lett.* **103**, 122405 (2013).
- [22] H.-H. Chen, C.-M. Lee, J.-C. Wu, L. Horng, C.-R. Chang, and J.-H. Chang, Synchronization of spin torque nano-oscillators through dipolar interactions, *J. Appl. Phys.* **115**, 134306 (2014).
- [23] H.-H. Chen, C.-M. Lee, Z. Zhang, Y. Liu, J.-C. Wu, L. Horng, and C.-R. Chang, Phase locking of spin-torque nano-oscillator pairs with magnetic dipolar coupling, *Phys. Rev. B* **93**, 224410 (2016).
- [24] A. Pikovsky, J. Kurths, and M. Rosenblum, *Synchronization: A Universal Concept in Nonlinear Sciences* (Cambridge University Press, New York, 2001).
- [25] F. Abreu Araujo and J. Grollier, Controlling the synchronization properties of two dipolarly coupled vortex based spin-torque nano-oscillators by the intermediate of a third one, *J. Appl. Phys.* **120**, 103903 (2016).
- [26] T. Taniguchi, Phase dynamics of oscillating magnetizations coupled via spin pumping, *Phys. Rev. B* **97**, 184408 (2018).
- [27] T. Taniguchi, S. Tsunegi, and H. Kubota, Mutual synchronization of spin-torque oscillators consisting of perpendicularly magnetized free layers and in-plane magnetized pinned layers, *APEX* **11**, 013005 (2018).
- [28] K. D. Hyung and S. Mincheol, Phase difference dependence of output power in synchronized stacked spin Hall nano-oscillators, *J. Phys.: Condens. Matter* **30**, 284001 (2018).
- [29] M. Zhang, L. Wang, D. Wei, and K.-Z. Gao, State diagram of magnetostatic coupling phase-locked spin-torque oscillators, *J. Appl. Phys.* **117**, 17D922 (2015).
- [30] D. Mancilla-Almonacid, R. E. Arias, R. A. Escobar, D. Altbir, and S. Allende, Spin wave modes of two magnetostatic coupled spin transfer torque nano-oscillators, *J. Appl. Phys.* **124**, 162102 (2018).
- [31] I. D. Mayergoyz, G. Bertotti, and C. Serpico, *Nonlinear Magnetization Dynamics in Nanosystems* (Elsevier, Oxford, 2009).
- [32] S. H. Strogatz, *Nonlinear Dynamics and Chaos: with Applications to Physics, Biology, Chemistry, and Engineering* (Westview Press, Boulder, CO, 2015).
- [33] W. H. Press, S. A. Teukolsky, W. T. Vetterling, and B. P. Flannery, *Numerical Recipes in C: the Art of Scientific Computing* (Cambridge University Press, New York, 1992).